

## Dirichlet-to-Neumann Map Method with Boundary Cells for Photonic Crystals Devices

Jianhua Yuan<sup>1,\*</sup> and Ya Yan Lu<sup>2</sup>

<sup>1</sup> *Department of Mathematics, Beijing University of Posts and Telecommunications, Beijing 100876, China.*

<sup>2</sup> *Department of Mathematics, City University of Hong Kong, Kowloon, Hong Kong.*

Received 25 September 2009; Accepted (in revised version) 23 April 2010

Available online 5 August 2010

---

**Abstract.** In a two-dimensional (2D) photonic crystal (PhC) composed of circular cylinders (dielectric rods or air holes) on a square or triangular lattice, various PhC devices can be created by removing or modifying some cylinders. Most existing numerical methods for PhC devices give rise to large sparse or smaller but dense linear systems, all of which are expensive to solve if the device is large. In a previous work [Z. Hu et al., *Optics Express*, 16 (2008), 17383-17399], an efficient Dirichlet-to-Neumann (DtN) map method was developed for general 2D PhC devices with an infinite background PhC to take full advantage of the underlying lattice structure. The DtN map of a unit cell is an operator that maps the wave field to its normal derivative on the cell boundary and it allows one to avoid computing the wave field in the interior of the unit cell. In this paper, we extend the DtN map method to PhC devices with a finite background PhC. Since there is no bandgap effect to confine the light in a finite PhC, a different technique for truncating the domain is needed. We enclose the finite structure with a layer of empty boundary and corner unit cells, and approximate the DtN maps of these cells based on expanding the scattered wave in outgoing plane waves. Our method gives rise to a relatively small and sparse linear systems that are particularly easy to solve.

**AMS subject classifications:** 78M25, 78M16, 78A45

**Key words:** Photonic crystal, Dirichlet-to-Neumann map, numerical simulation.

---

## 1 Introduction

Due to its periodic variation of the refractive index, a photonic crystal (PhC) [1] exhibits unusual dispersion properties and frequency intervals (i.e., bandgaps), in which propagating Bloch waves do not exist. Using the bandgap effect, waveguides and microcavities

---

\*Corresponding author. *Email addresses:* jianhua\_yuan@126.com (J. Yuan), mayylu@cityu.edu.hk (Y. Y. Lu)

can be created by introducing line or point defects. In a PhC waveguide, high transmission through a sharp bend is possible [2]. Microcavities in PhCs can have very high quality factors and small mode volumes. When waveguides and cavities are combined, many PhC devices can be developed. Some examples are frequency filters [3], channel drop filters [4], waveguide branches [5], waveguide couplers [3], Mach-Zehnder interferometers [6], etc. The unusual dispersion properties and nonlinear optical effects can be used to further develop useful PhC devices.

To analyze, design and optimize PhC devices, numerical simulations are essential. Unlike the eigenvalue problem for the band structure of a perfectly periodic and infinite PhC, mathematical problems associated with a PhC device are boundary value problems in the frequency domain or initial and boundary value problems in the time domain, and they must be solved in a much larger computation domain (compared with the unit cell) using proper boundary conditions. Although different time domain methods exist [3], many authors have used the finite difference time domain (FDTD) method [7] for simulating PhC devices. For problems such as the propagation of a pulse in the device, a time domain approach is essential. However, FDTD is often used for other problems, such as the transmission and reflection spectra of a PhC device, which are more naturally formulated in the frequency domain. One reason is that FDTD is easy to understand and widely available in existing software packages. Another reason is that standard frequency domain methods, such as the finite element [8] and finite difference (in frequency domain) methods, often give rise to large, indefinite and complex linear systems that are expensive to solve. However, FDTD often requires prohibitive computer resources and produces solutions of limited accuracy.

In the frequency domain, special numerical methods can be developed to take advantage of the geometric features of the PhC devices. For ideal two-dimensional (2D) PhC devices, we can identify three geometric features: the refractive index function is piecewise constant, often with only two different values; the PhC and the defect structures are often composed of circular cylinders surrounded by a homogeneous medium, where the cylinders are either air-holes or dielectric rods; the cylinders, include the defects, often form a square or triangular lattice. A number of existing numerical methods can take advantage at least some of these geometric features. The boundary integral equation (BIE) method [9] can take advantage of first feature. We can formulate integral equations for functions defined on the dielectric interfaces. The multipole method [10–13] can take advantage of the first and second features. Around a circular cylinder, we can write down the solution in cylindrical wave expansions and solve for the coefficients. The Dirichlet-to-Neumann (DtN) map method, first developed in [14] and [15], can take advantage of all three features.

The DtN map of a unit cell  $\Omega$  is the operator that maps the wave field to its normal derivative on the boundary of  $\Omega$ , and it can be approximated by a small matrix. Using the DtN maps of the unit cells, we can reduce various mathematical problems for PhCs to smaller problems on the edges of the unit cells, avoiding the interiors of the unit cells completely. In earlier works, the DtN map technique has been applied to eigenvalue

problems such as band structures [14, 16], waveguide modes [17] and cavity modes [18], and it has also been applied to boundary value problems involving PhCs of finite thickness [15, 19, 20] and PhC devices with an infinite PhC background [21, 22]. In this paper, we extend the DtN map method to PhC devices in a finite PhC surrounded by a homogeneous medium. Since the structures are not periodic, we cannot reduce the computation domain to one period as in [15]. Unlike the cases studied in [21], in the homogeneous medium outside the finite PhC, there is no bandgap effect to confine the light. Therefore, light waves can be scattered out in all directions and they need careful treatment at the boundary of the computation domain. Our approach is to enclose the finite PhC structure by one layer of empty unit cells, and develop special DtN maps for these boundary cells to simulate the outgoing radiation condition. As a result, we obtain a sparse linear system for the wave field on all edges of the unit cells in the computation domain. In contrast, the BIE and multipole methods give rise to linear systems with dense coefficient matrices.

## 2 DtN map method

For ideal 2D structures that are invariant in the  $z$ -direction and for waves propagating in the  $xy$ -plane, the frequency domain Maxwell's equations can be reduced to scalar Helmholtz equations for the two main polarizations. For the  $E$ -polarization, the  $z$  component of the electric field, denoted by  $u$ , satisfies

$$\frac{\partial^2 u}{\partial x^2} + \frac{\partial^2 u}{\partial y^2} + k_0^2 n^2 u = 0, \quad (2.1)$$

where  $k_0 = \omega/c$  is the free space wavenumber,  $\omega$  is the angular frequency (for the time dependence  $e^{-i\omega t}$ ),  $c$  is the speed of light in vacuum and  $n = n(x, y)$  is the refractive index function. The case of  $H$ -polarization is similar.

We consider PhC devices consisting of finite number of circular cylinders surrounded by a homogeneous medium with refractive index  $n_0$ , where the centers of the cylinders are located at lattice points of a square or triangular lattice. A typical example is shown in Fig. 1, where the cylinders (dielectric rods) are given on a square lattice and the missing cylinders form a waveguide bend [2]. For such a structure, we specify an incident wave  $u^{(i)}$  which satisfies the Helmholtz equation for the homogeneous medium with  $n = n_0$ . The objective is to find the scattered wave  $u^{(s)}$ , such that the total field

$$u = u^{(i)} + u^{(s)},$$

satisfies the Helmholtz equation (2.1) and  $u^{(s)}$  satisfies the Sommerfeld radiation condition at infinity

$$\lim_{r \rightarrow \infty} \frac{1}{\sqrt{r}} \left[ \frac{\partial u^{(s)}}{\partial r} - ik_0 n_0 u^{(s)} \right] = 0, \quad (2.2)$$

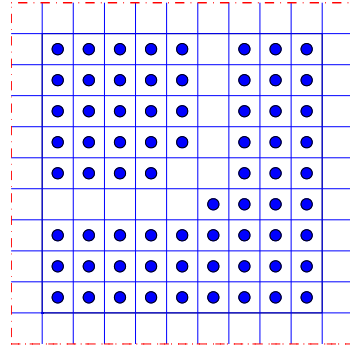


Figure 1: A  $90^\circ$  PhC waveguide bend in a finite PhC consisting of circular dielectric rods on a square lattice.

where  $r = \sqrt{x^2 + y^2}$  is the radial variable in a polar coordinate system. Eqs. (2.1) and (2.2) give rise to a standard scattering problem posed on the entire  $xy$ -plane.

In order to take advantage of the underlying lattice structure, we divide the domain into unit cells. The structure shown in Fig. 1 can be covered by a square domain containing  $9 \times 9$  unit cells. For this particular example, there are only two different types of unit cells: the regular unit cell with a circular cylinder and the defect (or empty) unit cell without the cylinder. To approximate the outgoing scattered wave, we introduce a layer of empty unit cells surrounding the structure. Therefore, the computation domain contains  $11 \times 11$  unit cells as shown in Fig. 1.

The DtN map of a unit cell  $\Omega$  is the operator  $\Lambda$  satisfying

$$\Lambda u = \frac{\partial u}{\partial \nu}, \quad \text{on } \partial\Omega,$$

where  $u$  is any solution of Eq. (2.1),  $\partial\Omega$  is the boundary of the  $\Omega$ , and  $\nu$  is unit normal vector of  $\partial\Omega$ . For the square unit cells shown in Fig. 1, we can replace  $\partial_\nu$  by  $\partial_x$  or  $\partial_y$  on vertical or horizontal edges, respectively. If we choose  $P$  points on each edge of a square unit cell,  $\Lambda$  can be approximated by a  $(4P) \times (4P)$  matrix based on cylindrical wave expansions [14, 15]. If the unit cell contains more than one cylinder or the cross section of the cylinder is not circular, the DtN map  $\Lambda$  can be approximated by the methods developed in [23] and [24], respectively. To actually write down a matrix approximation of  $\Lambda$ , we need to order the four edges of  $\Omega$ . We follow the ordering such that

$$u|_{\partial\Omega} = [u_{lower}; u_{left}; u_{right}; u_{upper}], \quad (2.3)$$

is a column vector with four blocks, where  $u_{left}$  denotes  $u$  on the left edge of  $\Omega$ , etc. The DtN map  $\Lambda$  is then given as a matrix in  $4 \times 4$  blocks, where each block  $\Lambda_{jk}$  (for  $1 \leq j, k \leq 4$ ) is a  $P \times P$  matrix. Using the DtN maps of the unit cells, we can establish a linear system for the wave field on all interior edges of the unit cells in the computation domain. To illustrate the procedure, we consider six unit cells in the lower left corner of the computation domain shown in Fig. 1 and label the six unit cells from 1 to 6 and their edges (in

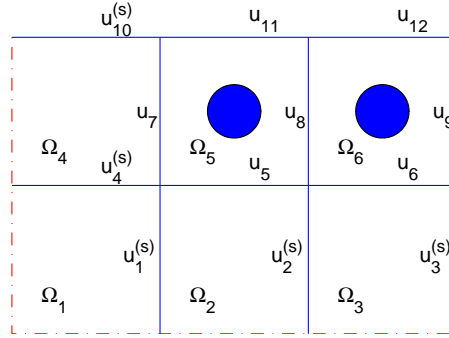


Figure 2: Six unit cells at the lower left corner of the computation domain for the 90° bend shown in Fig. 1.

the interior of the computation domain) from 1 to 12 as in Fig. 2. The eighth edge is the common edge of two interior unit cells  $\Omega_5$  and  $\Omega_6$ . If we denote the DtN map of  $\Omega_j$  by  $\Lambda^{(j)}$  and evaluate the  $x$  derivative of  $u$  on the eighth edge using both  $\Lambda^{(5)}$  and  $\Lambda^{(6)}$ , then

$$\Lambda_{31}^{(5)} u_5 + \Lambda_{32}^{(5)} u_7 + \Lambda_{33}^{(5)} u_8 + \Lambda_{34}^{(5)} u_{11} = \Lambda_{21}^{(6)} u_6 + \Lambda_{22}^{(6)} u_8 + \Lambda_{23}^{(6)} u_9 + \Lambda_{24}^{(6)} u_{12}, \quad (2.4)$$

where  $u_j$  denotes  $u$  on the  $j$ th edge. The above equation connects the seven edges in the two neighboring square unit cells. Notice that the third row of  $\Lambda^{(5)}$  is used in the left hand side of Eq. (2.4), since the eighth edge is the third edge of  $\Omega_5$ . The above procedure was previously used to compute defect modes in PhCs [18] and to analyze PhC devices in an infinite PhC background (with PhC waveguides extending to infinity) [21], where non-local boundary conditions that involve all unit cells along the relevant boundary segments are used to terminate PhC waveguides. The finite PhC structures in this paper require a different treatment for the boundary conditions.

For a boundary unit cell, such as  $\Omega_2$ ,  $\Omega_3$  and  $\Omega_4$  in Fig. 2, we can find an approximate DtN map that gives a relation between  $u^{(s)}$  and its normal derivative on three edges (all interior edges of the computation domain). For  $\Omega_2$ , the DtN map  $\Lambda^{(2)}$  satisfies

$$\Lambda^{(2)} \begin{bmatrix} u_1^{(s)} \\ u_2^{(s)} \\ u_5^{(s)} \end{bmatrix} = \begin{bmatrix} \partial_x u_1^{(s)} \\ \partial_x u_2^{(s)} \\ \partial_y u_5^{(s)} \end{bmatrix}. \quad (2.5)$$

In the discrete case,  $\Lambda^{(2)}$  is given in  $3 \times 3$  blocks, where each block is a  $P \times P$  matrix. For a corner unit cell, we look for a DtN map that links  $u^{(s)}$  and  $\partial_\nu u^{(s)}$  on the two interior edges. For  $\Omega_1$ , the DtN map  $\Lambda^{(1)}$  satisfies

$$\Lambda^{(1)} \begin{bmatrix} u_1^{(s)} \\ u_4^{(s)} \end{bmatrix} = \begin{bmatrix} \partial_x u_1^{(s)} \\ \partial_y u_4^{(s)} \end{bmatrix}. \quad (2.6)$$

When discretized,  $\Lambda^{(1)}$  is a  $(2P) \times (2P)$  matrix given in  $2 \times 2$  blocks. Notice that the DtN maps for the boundary and corner unit cells are defined for the scattered field (instead of the total field). In Section 3, we present a method for computing these DtN maps.

On each edge of the boundary or corner unit cells, we can establish an equation as before. However, some care is needed since the scattered field is used for these unit cells. We choose to use the total field on common edges between interior and boundary unit cells, and use the scattered field on common edges between boundary cells or corner cells. For the cells shown in Fig. 2, we establish equations for  $u_1^{(s)}, u_2^{(s)}, u_3^{(s)}, u_4^{(s)}, u_{10}^{(s)}$ , and  $u_5, u_6, u_7$ , etc. For the first edge, we evaluate  $\partial_x u_1^{(s)}$  by the DtN maps of  $\Omega_1$  and  $\Omega_2$ , and obtain

$$\Lambda_{11}^{(1)} u_1^{(s)} + \Lambda_{12}^{(1)} u_4^{(s)} = \Lambda_{11}^{(2)} u_1^{(s)} + \Lambda_{12}^{(2)} u_2^{(s)} + \Lambda_{13}^{(2)} [u_5 - u_5^{(i)}]. \quad (2.7)$$

Notice that  $u_5^{(s)}$  is replaced by  $u_5 - u_5^{(i)}$ . Therefore, the above is an inhomogeneous equation involving  $u_1^{(s)}, u_2^{(s)}, u_4^{(s)}$  and  $u_5$ . For the second edge, we have

$$\Lambda_{21}^{(2)} u_1^{(s)} + \Lambda_{22}^{(2)} u_2^{(s)} + \Lambda_{23}^{(2)} [u_5 - u_5^{(i)}] = \Lambda_{11}^{(3)} u_2^{(s)} + \Lambda_{12}^{(3)} u_3^{(s)} + \Lambda_{13}^{(3)} [u_6 - u_6^{(i)}]. \quad (2.8)$$

For the fifth edge, we evaluate  $\partial_y u_5$  by  $\Lambda^{(5)}$  and  $\partial_y u_5^{(s)}$  by  $\Lambda^{(2)}$ . Therefore, we need to add  $\partial_y u^{(i)}$  to establish the following equation:

$$\Lambda_{31}^{(2)} u_1^{(s)} + \Lambda_{32}^{(2)} u_2^{(s)} + \Lambda_{33}^{(2)} [u_5 - u_5^{(i)}] + \partial_y u_5^{(i)} = \Lambda_{11}^{(5)} u_5 + \Lambda_{12}^{(5)} u_7 + \Lambda_{13}^{(5)} u_8 + \Lambda_{14}^{(5)} u_{11}. \quad (2.9)$$

The above is an inhomogeneous equation involving  $u_1^{(s)}, u_2^{(s)}, u_5, u_7, u_8$  and  $u_{11}$ .

Since the incident field propagates in certain directions, it is possible that  $u^{(i)}$  is also an outgoing field in certain boundary and corner unit cells. In that case, the total field  $u$  also satisfies (2.5) or (2.6), and it can be used to establish the equations. The equations involving only the total field is always homogeneous. Of course,  $u^{(i)}$  must be an incoming field on some boundary or corner unit cells, where the DtN maps are only applicable to  $u^{(s)}$ .

It is clear that the equation for each edge involves only the edges in the two neighboring unit cells. Therefore, the final linear system for all edges in the computation domain is sparse. This is different from the cases studied in [21], where non-local boundary conditions for PhC waveguides partially destroy the sparsity of the coefficient matrix. This is also the main advantage of our method when it is compared with the multipole and boundary integral equation methods, since the coefficient matrices appeared in these methods are dense.

### 3 DtN maps of boundary and corner cells

From the previous section, it is clear that the DtN maps of the unit cells are the key elements of our method. For an interior unit cell with a circular cylinder or an empty

interior unit cell, the DtN map can be constructed using cylindrical wave expansions [14, 15]. For more complicated unit cells, the DtN maps can be constructed using related numerical solutions of the Helmholtz equation [23,24]. For a square unit cell, if  $P$  points are used on each edge, then the field in the unit cell is approximated by a sum of  $4P$  special solutions and the DtN map is approximated by a  $(4P) \times (4P)$  matrix.

For boundary and corner unit cells, the DtN maps can be constructed based on approximating the scattered field by outgoing plane waves. Consider the unit cells at the lower boundary of the truncated domain, such as  $\Omega_2$  and  $\Omega_3$  in Fig. 2, if the upper edges of these cells are located at  $y=y_1$ , then the scattered wave for  $y < y_1$  are down-going plane waves

$$u^{(s)}(x,y) = \int_{-\infty}^{\infty} c(\alpha) e^{i(\alpha x - \beta y)} d\alpha, \quad y < y_1, \tag{3.1}$$

where  $\beta = \sqrt{k_0^2 n_0^2 - \alpha^2}$  and  $c(\alpha)$  is related to the Fourier transform of  $u^{(s)}(x, y_1)$ . Here,  $\beta$  is defined such that

$$\beta = i \sqrt{\alpha^2 - k_0^2 n_0^2}, \quad \text{if } |\alpha| > k_0 n_0,$$

therefore  $u^{(s)}$  given in (3.1) includes evanescent plane waves that decay exponentially as  $y \rightarrow -\infty$ . To obtain an approximate DtN map for  $\Omega_2$ , we replace (3.1) by

$$u^{(s)}(x,y) \approx \sum_{m=1}^{3P} c_m e^{i(\alpha_m x - \beta_m y)}, \quad y < y_1, \tag{3.2}$$

where  $\alpha_m$ , for  $1 \leq m \leq 3P$ , are uniformly sampled from the interval  $(-\alpha_*, \alpha_*)$  for some  $\alpha_*$  and  $\beta_m = \sqrt{k_0^2 n_0^2 - \alpha_m^2}$ . Typically, we choose  $\alpha_*$ , such that

$$4 \leq \frac{\alpha_*}{k_0 n_0} \leq 6.$$

On the left, right and upper edges of  $\Omega_2$ , we choose  $3P$  points uniformly (avoiding the corners) and evaluate  $u^{(s)}$  at these points using (3.2). This gives rise to a matrix  $C$  that maps the coefficients  $\{c_m\}$  to the  $3P$  values of  $u^{(s)}$  on the boundary. Similarly, we evaluate the normal derivative of  $u^{(s)}$  at these  $3P$  points using (3.2), and obtain a matrix  $D$  that maps  $\{c_m\}$  to the normal derivatives. Therefore, we obtain the following approximate DtN map of  $\Omega_2$ :

$$\Lambda^{(2)} = DC^{-1}. \tag{3.3}$$

Since all boundary unit cells below the line  $y = y_1$  are identical, so are their DtN maps. Therefore, we have

$$\Lambda^{(3)} = \Lambda^{(2)},$$

etc. For boundary unit cells at the left, right or upper boundaries of the truncated domain, we can construct their DtN maps using similar expansions in outgoing plane waves. Alternatively, the DtN maps of these boundary unit cells can be obtained from  $\Lambda^{(2)}$  using simple matrix transforms.

The DtN map of a corner unit cell can be constructed by the same approach. We consider the lower-left corner unit cell  $\Omega_1$  whose right and upper edges are assumed to be given at  $x = x_1$  and  $y = y_1$ , respectively. To maintain the symmetry between  $x$  and  $y$ , we rotate the coordinate axes by  $-45^\circ$ , so that a point  $(x, y)$  becomes  $(x', y')$  given by

$$x' = \frac{1}{\sqrt{2}}(x - y), \quad y' = \frac{1}{\sqrt{2}}(x + y). \quad (3.4)$$

In the half plane given by

$$x + y < x_1 + y_1 \quad \left( \text{or } y' < \frac{x_1 + y_1}{\sqrt{2}} \right),$$

the scattered field can be written as

$$u^{(s)}(x, y) = \int_{-\infty}^{\infty} c(\alpha) e^{i(\alpha x' - \beta y')} d\alpha, \quad y' < \frac{x_1 + y_1}{\sqrt{2}}, \quad (3.5)$$

where  $c(\alpha)$  is related to the Fourier transform of  $u^{(s)}$  evaluated on the line  $x + y = x_1 + y_1$ . To construct the DtN map for  $\Omega_1$ , we approximate  $u^{(s)}$  by  $2P$  plane waves

$$u^{(s)}(x, y) \approx \sum_{m=1}^{2P} c_m e^{i(\alpha_m x' - \beta_m y')}, \quad y' < \frac{x_1 + y_1}{\sqrt{2}}, \quad (3.6)$$

where  $\alpha_m$ , for  $1 \leq m \leq 2P$ , are uniformly sampled from the interval  $(-\alpha_*, \alpha_*)$  and  $\beta_m$  is defined as before. To obtain the matrix  $\Lambda^{(1)}$ , we choose  $2P$  points uniformly on the right and upper edges of  $\Omega_1$ , and calculate  $u^{(s)}$  and its normal derivative at these  $2P$  points using (3.6). This gives rise to two  $(2P) \times (2P)$  matrices similar to the matrices  $C$  and  $D$  above. The DtN map  $\Lambda_1^{(1)}$  is then obtained from these two matrices by a formula similar to (3.3). The DtN maps of the other corner unit cells can be constructed similarly or obtained from  $\Lambda^{(1)}$  directly through suitable matrix transforms.

The number of sampling points  $P$  on each edge of the unit cells is typically quite small. This is related to the fact that the wave field in each interior unit cell is approximated by  $4P$  cylindrical waves. Since the typical size of the unit cells is smaller than the free space wavelength, a small  $P$  such as  $P = 7$ , is usually sufficient. On the other hand, if a larger  $P$  is used, the construction of the DtN maps for the boundary and corner unit cells may encounter some difficulties, due to the possible near linear dependence of the plane waves evaluated at the boundary points. More precisely, the matrix  $C$  appeared in (3.3) may be near singular, then  $\Lambda^{(2)}$  cannot be obtained accurately. This difficulty can be partially overcome by a sub-cell approach. The idea is to divide a boundary or corner unit cell as four smaller sub-cells, then calculate the DtN maps of the sub-cells and use them to obtain the DtN map of the original unit cell. The sub-cells for  $\Omega_1$  and  $\Omega_2$  are depicted in Fig. 3. We observe that  $\Omega_1$  has one interior sub-cell  $\Omega_1^{22}$ , two boundary sub-cells  $\Omega_1^{12}$  and  $\Omega_1^{21}$ , and one corner sub-cell  $\Omega_1^{11}$ , and  $\Omega_2$  has two interior sub-cells and

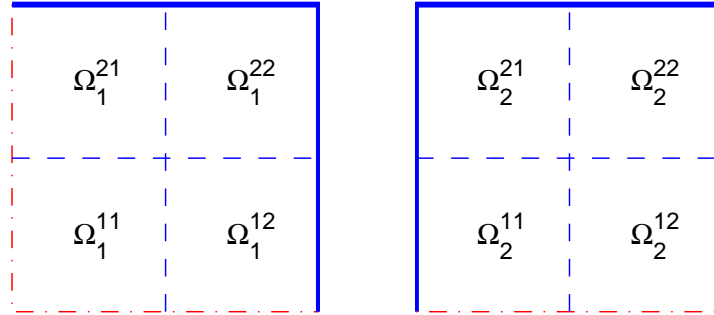


Figure 3: Sub-cells for the corner unit cell  $\Omega_1$  and the boundary unit cell  $\Omega_2$ .

two boundary sub-cells. The DtN maps of the sub-cells can be obtained by the method described above using  $P/2$  points on each edge, assuming that  $P$  is an even integer. Based on these DtN maps of the sub-cells, we can eliminate the field on the interior edges shown as the dashed lines in Fig. 3, and then obtain the DtN maps of the original unit cell. As an example, we consider  $\Omega_1$ . Using the DtN maps of the four sub-cells, we have

$$\begin{bmatrix} \partial_x u_1^{(s)} \\ \partial_y u_4^{(s)} \end{bmatrix} = A_1 \begin{bmatrix} u_1^{(s)} \\ u_4^{(s)} \end{bmatrix} + A_2 v, \tag{3.7}$$

where  $v$  is a vector of length  $2P$  representing  $u^{(s)}$  on the four interior edges of the sub-cells in  $\Omega_1$ ,  $A_1$  and  $A_2$  are  $(2P) \times (2P)$  matrices. As in Fig. 2, the right and upper edges of  $\Omega_1$  are the first and fourth edges, respectively. Meanwhile, we can establish equations for  $u^{(s)}$  on the interior edges by evaluating its normal derivative using the DtN maps of the two neighboring sub-cells. This gives rise to

$$A_3 v = A_4 \begin{bmatrix} u_1^{(s)} \\ u_4^{(s)} \end{bmatrix},$$

where  $A_3$  and  $A_4$  are  $(2P) \times (2P)$  matrices. Solving  $v$  from the above equation and substituting the solution into (3.7), we obtain the DtN map of  $\Omega_1$

$$\Lambda^{(1)} = A_1 + A_2 A_3^{-1} A_4.$$

Clearly, the DtN maps of  $\Omega_2$  or any other boundary or corner unit cells can be similarly obtained from the DtN maps of the sub-cells.

To assess the accuracy of the DtN maps for boundary and corner unit cells, we test the DtN maps on a few exact solutions. For the unit cell  $\Omega_2$  shown in Fig. 2, we choose four exact solutions which are cylindrical waves originated from the centers of the  $\Omega_5$  and  $\Omega_6$ .

Let  $\mathbf{c}_5$  and  $\mathbf{c}_6$  be the centers of  $\Omega_5$  and  $\Omega_6$ , respectively, then the four special solutions are

$$U_1(\mathbf{r}) = H_0^{(1)}(k_0 n_0 |\mathbf{r} - \mathbf{c}_5|), \quad (3.8a)$$

$$U_2(\mathbf{r}) = H_0^{(1)}(k_0 n_0 |\mathbf{r} - \mathbf{c}_6|), \quad (3.8b)$$

$$U_3(\mathbf{r}) = H_1^{(1)}(k_0 n_0 |\mathbf{r} - \mathbf{c}_5|) \exp(i\theta_5), \quad (3.8c)$$

$$U_4(\mathbf{r}) = H_1^{(1)}(k_0 n_0 |\mathbf{r} - \mathbf{c}_6|) \exp(i\theta_6), \quad (3.8d)$$

where  $\mathbf{r} = (x, y)$ ,  $\theta_5$  and  $\theta_6$  are the polar angles of  $\mathbf{r} - \mathbf{c}_5$  and  $\mathbf{r} - \mathbf{c}_6$ , respectively. For each special solution  $U_j$  and a given integer  $P$ , we can evaluate its normal derivative  $\partial_\nu U_j$  at the  $3P$  sampling points on the three interior edges of  $\Omega_2$  exactly. We can also approximate  $\partial_\nu U_j$  at these  $3P$  points by the DtN map of  $\Omega_2$ . Then, we can calculate the relative error  $E_j$  for  $\partial_\nu U_j$  at these  $3P$  points using the vector 2-norm. For  $\omega L / (2\pi c) = 0.353$ ,  $n_0 = 1$  and  $\alpha_* = 6k_0 n_0$ , where  $L$  is the length of the edges of the square unit cells, we obtain the relative errors listed in Table 1. We observe that the relative errors tend to decrease as  $P$  is increased up to  $P=9$ . Roughly 3 digits of accuracy can be obtained for  $P=7, 8$  and  $9$ . Additional calculations are performed for other values of  $\alpha_*$  satisfying

$$4k_0 n_0 \leq \alpha_* \leq 6k_0 n_0.$$

It appears that the best value of  $\alpha_*$  should increase as  $P$  is increased. Unfortunately, the errors cannot be reduced by further increasing  $P$ . One reason is that the boundary DtN map is only a local approximation (at the level of a unit cell) to the exact non-local outgoing radiation condition. In addition, for a larger  $P$ , the construction the DtN map becomes ill-conditioned, since the plane waves with nearly identical wave vectors are nearly linearly dependent.

Table 1: Relative errors of the normal derivatives on three edges of  $\Omega_2$  calculated by the DtN map for four special solutions.

$P$	$E_1$	$E_2$	$E_3$	$E_4$
5	0.0318	0.4129	0.1912	0.2859
6	0.0397	0.0206	0.0280	0.0457
7	0.0037	0.0046	0.0031	0.0055
8	0.0029	0.0014	0.0019	0.0035
9	0.0006	0.0007	0.0030	0.0012
10	0.0013	0.0007	0.0019	0.0016

For the corner unit cell  $\Omega_1$ , we test the accuracy of its DtN map by computing  $\partial_\nu U_j$  on the two interior edges. The first three exact solutions are used and the relative errors are similarly defined. For  $\omega L / (2\pi c) = 0.353$ ,  $n_0 = 1$  and  $\alpha_* = 4k_0 n_0$ , the results are given in Table 2. Since only  $2P$  plane waves are used to construct the DtN map of the corner unit cell, the relative errors are larger. Roughly two significant digits can be obtained in these calculations. Since the wave field at the corners are typically very weak, the lower

Table 2: Relative errors of the normal derivatives on two edges of  $\Omega_1$  calculated by the DtN map for three special solutions.

$P$	$E_1$	$E_2$	$E_3$
5	0.1252	0.0682	0.0832
6	0.1686	0.0794	0.1108
7	0.0415	0.0179	0.0273
8	0.0265	0.0106	0.0144
9	0.0205	0.0083	0.0320
10	0.0477	0.0105	0.2256

accuracy of corner DtN maps should not significantly reduce the accuracy of the final solution.

## 4 Numerical examples

In this section, we apply our method to analyze a number of finite PhC structures consisting of circular dielectric rods on a square lattice, where the refractive index of the rods is  $n = 3.4$ , the medium surrounding the rods is air (thus  $n_0 = 1$ ), the radius of the rods is  $a = 0.18L$  and  $L$  is the lattice constant. It is known that the bulk PhC has a bandgap given by  $0.302 < \omega L / (2\pi c) < 0.443$  for the  $E$ -polarization. If a row of rods is removed, a PhC waveguide is formed and it has a single propagating Bloch mode for  $0.312 < \omega L / (2\pi c) < 0.443$ .

Our first example is a finite version of the  $90^\circ$  PhC waveguide bend proposed by Mekis et al. [2]. A small version of the structure is shown in Fig. 1. In principle, the ideal bend is a defect structure embedded in an infinite PhC where the waveguide extends to infinity in the negative  $x$  and positive  $y$ -directions. In an earlier work [21], the DtN map method was used to analyze this ideal bend based on rigorous (but non-local) boundary conditions for terminating the semi-infinite PhC waveguides. In the following, we consider a bending structure in a finite PhC involving  $16 \times 15$  unit cells (larger than the  $9 \times 9$  structure shown in Fig. 1). Since we enclose the structure with a layer of empty unit cells, the actual computation domain involves  $18 \times 17$  unit cells. For simplicity, we choose the  $xy$  coordinates, such that the computation domain is given by  $0 < x < 18L$  and  $0 < y < 17L$ . Furthermore, the unit cells are bounded and separated by vertical and horizontal lines given by

$$x = x_j \quad \text{and} \quad y = y_k, \quad \text{for} \quad 0 \leq j \leq 18 \quad \text{and} \quad 0 \leq k \leq 17,$$

where

$$x_j = jL \quad \text{and} \quad y_k = kL.$$

For this problem, we specify an incident field which is a Gaussian beam satisfying

$$u^{(i)} = e^{-[(y-y_*)/w]^2}, \quad x = x_1, \quad (4.1)$$

where  $w = 0.5L$  and  $y_*$  corresponds to the center of the horizontal waveguide. Besides (4.1),  $u^{(i)}$  also satisfies the Helmholtz equation for the homogeneous medium, where  $n = n_0$ . Since it is a beam propagating in the positive  $x$ -direction, it can be written as

$$u^{(i)} = \Phi e^{ik_0 n_0 x},$$

where  $\Phi$  is the slowly varying envelope satisfying the paraxial wave equation. As a result, we have

$$\frac{\partial u^{(i)}}{\partial x} \approx ik_0 n_0 e^{-[(y-y_*)/w]^2} \left\{ 1 + \frac{2[(y-y_*)/w]^2 - 1}{k_0^2 n_0^2 w^2} \right\}, \quad x = x_1. \quad (4.2)$$

It is well known that this sharp waveguide bend exhibits high transmission for a large interval of frequencies. In particular, near 100% transmission can be realized at  $\omega L / (2\pi c) = 0.353$ . For this particular frequency, using  $P = 7$  points on each edge of the unit cells, we obtain the electric field pattern shown in Fig. 4. Nearly 100% transmission is observed, since the electric field has about the same magnitude in the incoming (horizontal) and outgoing (vertical) waveguides. However, even if we consider only the field around the bend in the PhC, the field pattern is not identical to that in the ideal bend [21], since there are reflected waves at the boundary of the structure where the PhC waveguide is terminated.

For this example, we compare the numerical solutions obtained with a few different values of  $P$  at three check points  $A$ ,  $B$  and  $C$ . These three points are located at the entrance, the center and the exit of the bent waveguide, respectively. In the computation domain given by  $0 < x < 18L$  and  $0 < y < 17L$ , the coordinates of  $A$ ,  $B$  and  $C$  are  $(1.5L, 6.5L)$ ,  $(9.5L, 7.5L)$ ,  $(10.5L, 16.5L)$ , respectively. Using  $\alpha_* = 6k_0 n_0$  for the boundary DtN maps and  $\alpha_* = 4k_0 n_0$  for the corner DtN maps, we obtain the results given in Table 3. It appears that the solutions are accurate to two or three digits for  $P = 7, 8$  and  $9$ , and they are consistent with the accuracy of the boundary and corner DtN maps. Although the accuracy of the solution is limited, we emphasize that the computation domain is quite small.

Table 3: Numerical solutions at the three points  $A$ ,  $B$  and  $C$  in the waveguide bend. The boundary and corner DtN maps are obtained with  $\alpha_* = 6k_0 n_0$  and  $\alpha_* = 4k_0 n_0$ , respectively.

$P$	$u _A$	$u _B$	$u _C$
7	0.4750+0.3992i	0.7067-0.4247i	0.9010-0.4494i
8	0.4790+0.3977i	0.7066-0.4256i	0.9017-0.4519i
9	0.4750+0.3967i	0.7062-0.4265i	0.9006-0.4534i

Next, we consider the Y branch and T branch previously analyzed by Koshiba et al. [3]. The structures are shown in Fig. 5. In our calculations, we assume that the two branches are embedded in a finite PhC involving  $17 \times 16$  unit cells. With the additional layer of empty unit cells surrounding the structure, our computation domain covers  $19 \times$

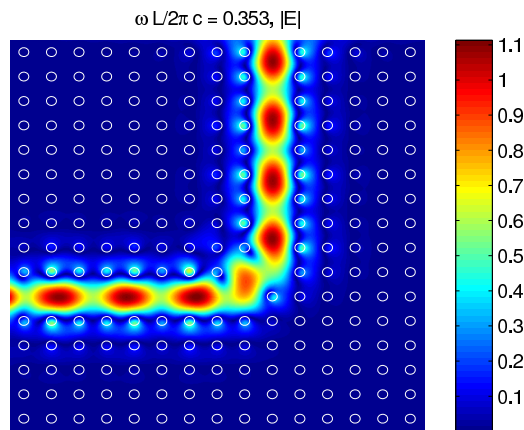


Figure 4: Magnitude of the electric field for the 90° PhC waveguide bend at  $\omega L/(2\pi c) = 0.353$ .

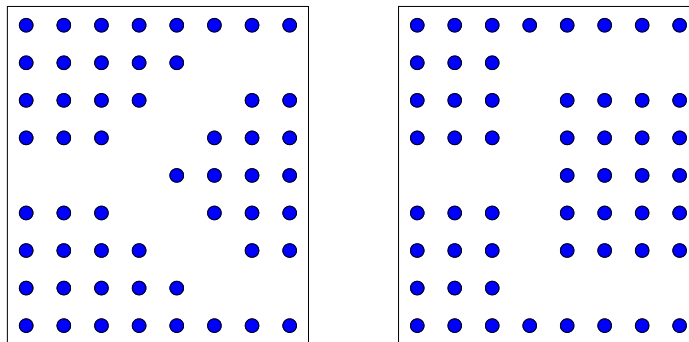


Figure 5: Y branch (left) and T branch (right) for photonic crystal waveguides.

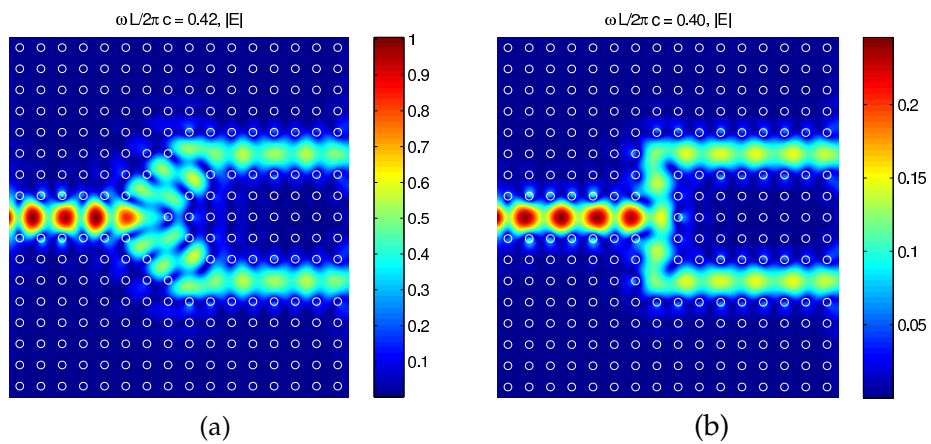


Figure 6: Magnitude of the electric field in the Y branch at  $\omega L/(2\pi c) = 0.42$  (a), and in the T branch at  $\omega L/(2\pi c) = 0.40$  (b).

18 unit cells. For this problem, we use the same incident field given earlier. For the Y branch and the normalized frequency  $\omega L/(2\pi c) = 0.42$ , we use  $P = 7$  for the number of points on each edge and obtain the electric field pattern shown in Fig. 6(a). For the T branch and the normalized frequency  $\omega L/(2\pi c) = 0.4$ , we use  $P = 5$  points on each edge and obtain the electric field pattern shown in Fig. 6(b). Our results are consistent with those given in [3]. It can be seen that the transmission is not as high as desired for both branches, but the T branch performs better than the Y branch. For the computation domain with  $19 \times 18$  unit cells, we have 647 interior edges. For  $P = 5$  and  $P = 7$ , the total number of unknowns is 3235 and 4529, respectively. However, the coefficient matrix is sparse, since each equation involves at most 7 edges, i.e.,  $7P$  unknowns.

## 5 Conclusions

In this paper, we developed an efficient DtN map method for finite 2D PhC devices. The structures analyzed consist of finite number of cylinders on a square lattice, where the cylinders are surrounded by a homogeneous medium. Although it is a standard multiple scattering problem, existing methods such as the multipole and boundary integral equation methods, fail to take advantage of the underlying lattice structure. Due to the existence of many identical unit cells, the DtN maps of the unit cells can be used to derive efficient numerical methods for various problems associated with PhCs. In particular, the DtN maps allow us to set up a linear system of equations for wave fields on the edges of the unit cells only. Compared with standard numerical methods (such as the finite element method) that discretize the 2D computation domain directly, the number of unknowns in our method is much smaller. Another main advantage of the DtN map method is that the coefficient matrix of the linear system is sparse. In contrast, the multipole and boundary integral equation methods give dense coefficient matrices, while the numbers of unknowns in these two methods are close to that of the DtN map method.

In a previous work [21, 22], the DtN map approach has been used to analyze PhC devices embedded in an infinite PhC with a few PhC waveguides extending to infinity. Rigorous boundary conditions were developed to terminate semi-infinite PhC waveguides [21]. These non-local boundary conditions partially destroy the sparsity of the coefficient matrix. The PhC devices considered in this paper are embedded in a finite PhC, where the medium away from the finite structure is homogeneous. Based on a layer of empty unit cells enclosing the finite PhC structure, we obtain a truly sparse linear system for wave fields on the edges of the unit cells. The key step is to construct the DtN maps of the boundary and corner unit cells for the scattered waves using expansions in outgoing plane waves. Numerical examples involving hundreds of unit cells (or cylinders) are used to illustrate the efficiency of our method.

The DtN maps for the boundary and corner unit cells are local at the level of unit cells, and they are used to approximate the true outgoing radiation condition which is non-local. As a result, the accuracy of these DtN maps cannot be continuously improved

by increasing  $P$  (the number of sampling points on each edge). Since we have used these boundary and corner DtN maps in the immediate neighborhood of the scatterers (the cylinders in the PhC), the overall accuracy of the numerical solution is also limited to two or three digits. In analog to the local absorbing boundary conditions, if we enlarge the computation domain with more layers of empty unit cells, the accuracy of the final solution could be improved, but it also increases the computational complexity. Currently, we are exploring various ways to improve the accuracy.

## Acknowledgments

This research was partially supported by the National Science Foundation of China (Project No. 10701016), the open fund of key laboratory of information photonics and optical communications (Beijing University of Posts and Telecommunications) of Ministry of Education, the fundamental research funds for the central universities (BUPT2009RC0706), and a grant from the Research Grants Council of Hong Kong Special Administrative Region, China (Project No. CityU 102207).

## References

- [1] J. D. Joannopoulos, R. D. Meade and J. N. Winn, *Photonic Crystals: Molding the Flow of Light*, Princeton University Press, Princeton, NJ, 1995.
- [2] A. Mekis, J. C. Chen, I. Kurland, S. Fan, P. R. Villeneuve and J. D. Joannopoulos, High transmission through sharp bends in photonic crystal waveguides, *Phys. Rev. Lett.*, 77 (1996), 3787–3790.
- [3] M. Koshiba, Y. Tsuji and M. Hikari, Time-domain beam propagation method and its application to photonic crystal circuits, *J. Lightw. Technol.*, 18 (2000), 102–110.
- [4] S. Fan, P. R. Villeneuve, J. D. Joannopoulos and H. A. Haus, Channel drop tunneling through localized states, *Phys. Rev. Lett.*, 80 (1998), 960–963.
- [5] S. Fan, S. G. Johnson, J. D. Joannopoulos, C. Manolatou and H. A. Haus, Waveguide branches in photonic crystals, *J. Opt. Soc. Am. B.*, 18 (2001), 162–165.
- [6] T. Fujisawa and M. Koshiba, Finite-element modeling of nonlinear interferometers based on photonic-crystal waveguides for all-optical signal processing, *J. Lightw. Technol.*, 24 (2006), 617–623.
- [7] A. Taflove and S. C. Hagness, *Computational Electrodynamics: the Finite-Difference Time-Domain Method*, 2nd ed., Artech House, 2000.
- [8] J. M. Jin, *The Finite Element Method in Electromagnetics*, 2nd ed., John Wiley & Sons, New York, 2002.
- [9] D. Colton and R. Kress, *Inverse Acoustic and Electromagnetic Scattering Theory*, 2nd ed., Springer-Verlag, Berlin, 1998.
- [10] D. Felbacq, G. Tayeb and D. Maystre, Scattering by a random set of parallel cylinders, *J. Opt. Soc. Am. A.*, 11 (1994), 2526–2538.
- [11] R. C. McPhedran, L. C. Botten, A. A. Asatryan et al., Calculation of electromagnetic properties of regular and random arrays of metallic and dielectric cylinders, *Phys. Rev. E.*, 60 (1999), 7614–7617.

- [12] L. C. Botten, T. P. White, A. A. Asatryan et al., Bloch mode scattering matrix methods for modeling extended photonic crystal structures. I: theory, *Phys. Rev. E.*, 70 (2004), 056606.
- [13] K. Yasumoto, H. Toyama and T. Kushta, Accurate analysis of two-dimensional electromagnetic scattering from multilayered periodic arrays of circular cylinders using lattice sums technique, *IEEE T. Antenn. Propag.*, 52 (2004), 2603–2611.
- [14] J. Yuan and Y. Y. Lu, Photonic bandgap calculations using Dirichlet-to-Neumann maps, *J. Opt. Soc. Am. A.*, 23 (2006), 3217–3222.
- [15] Y. Huang and Y. Y. Lu, Scattering from periodic arrays of cylinders by Dirichlet-to-Neumann maps, *J. Lightw. Technol.*, 24 (2006), 3448–3453.
- [16] J. Yuan and Y. Y. Lu, Computing photonic band structures by Dirichlet-to-Neumann maps: the triangular lattice, *Opt. Commun.*, 273 (2007), 114–120.
- [17] Y. Huang, Y. Y. Lu and S. Li, Analyzing photonic crystal waveguides by Dirichlet-to-Neumann maps, *J. Opt. Soc. Am. B.*, 24 (2007), 2860–2867.
- [18] S. Li and Y. Y. Lu, Computing photonic crystal defect modes by Dirichlet-to-Neumann maps, *Opt. Express.*, 15 (2007), 14454–14466.
- [19] Y. Huang and Y. Y. Lu, Modeling photonic crystals with complex unit cells by Dirichlet-to-Neumann maps, *J. Comput. Math.*, 25 (2007), 337–349.
- [20] Y. Wu and Y. Y. Lu, Dirichlet-to-Neumann map method for analyzing interpenetrating cylinder arrays in a triangular lattice, *J. Opt. Soc. Am. B.*, 25 (2008), 1466–1473.
- [21] Z. Hu and Y. Y. Lu, Efficient analysis of photonic crystal devices by Dirichlet-to-Neumann maps, *Opt. Express.*, 16 (2008), 17383–17399.
- [22] Z. Hu and Y. Y. Lu, Improved Dirichlet-to-Neumann map method for modeling extended photonic crystal devices, *Opt. Quant. Electron.*, 40 (2008), 921–932.
- [23] S. Li and Y. Y. Lu, Multipole Dirichlet-to-Neumann map method for photonic crystals with complex unit cells, *J. Opt. Soc. Am. A.*, 24 (2007), 2438–2442.
- [24] J. Yuan, Y. Y. Lu and X. Antoine, Modeling photonic crystals by boundary integral equations and Dirichlet-to-Neumann maps, *J. Comput. Phys.*, 227 (2008), 4617–3629.